Automated Landmarking and Geometric Characterization of the Carotid Siphon

Hrvoje Bogunović[a,b,*], José María Pozo[a,b], Rubén Cárdenes[a,b], María Cruz Villa-Uriol[a,b], Raphaël Blanc[c], Michel Piotin[c], Alejandro F. Frangi[a,b,d]

[a]*Center for Computational Imaging & Simulation Technologies in Biomedicine (CISTIB), Universitat Pompeu Fabra (UPF), Barcelona, Spain*
[b]*Networking Biomedical Research Center on Bioengineering, Biomaterials and Nanomedicine (CIBER-BBN), Barcelona, Spain*
[c]*Department of Interventional and Functional Neuroradiology, Foundation Rothschild Hospital, Paris, France*
[d]*Department of Mechanical Engineering, University of Sheffield, Sheffield, UK*

Abstract

The geometry of the carotid siphon has a large variability between subjects, which has prompted its study as a potential geometric risk factor for the onset of vascular pathologies on and off the internal carotid artery (ICA). In this work, we present a methodology for an objective and extensive geometric characterization of carotid siphon parameterized by a set of anatomical landmarks. We introduce a complete and automated characterization pipeline. Starting from the segmentation of vasculature from angiographic image and its centerline extraction, we first identify ICA by characterizing vessel tree bifurcations and training a support vector machine classifier to detect ICA terminal bifurcation. On ICA centerline curve, we detect anatomical landmarks of carotid siphon by modeling it as a sequence of four bends and selecting their centers and interfaces between them. Bends are detected from the trajectory of the curvature vector expressed in the parallel transport frame of the curve. Finally, using the detected landmarks, we characterize the geometry in two complementary ways. First, with a set of local and global geometric features, known to affect hemodynamics. Second, using large deformation diffeomorphic metric curve mapping (LDDMCM) to quantify pair-wise shape similarity. We processed 96 images acquired with 3D rotational angiography. ICA identification had a cross-validation success rate of 99%. Automated landmarking was validated by computing limits of agreement with the reference taken to be the locations of the manually placed landmarks averaged across multiple observers. For all but one landmark, either the bias was not statistically significant or the variability was within 50% of the inter-observer one. The subsequently computed values of geometric features and LDDMCM were commensurate to the ones obtained with manual landmarking. The characterization based on pair-wise LDDMCM proved better in classifying the carotid siphon shape classes than the one based on geometric features. The proposed characterization provides a rich description of geometry and is ready to be applied in the search for geometric risk factors of the carotid siphon.

Keywords: Cerebral angiography, Internal carotid artery, Segmentation, Geometric quantification, Computational anatomy, LDDMM, Landmarks.

1. Introduction

The locations where vascular pathologies tend to occur more frequently are in general non-uniformly distributed across the vasculature. For example, cerebral aneurysms (pathological bulging of arteries) have strong preference for occurring at specific locations, and are frequently found at or near the regions of high vascular curvature in arteries of the Circle of Willis (Brisman et al., 2006). Similarly, atherosclerosis (thickening of the arterial wall) often occurs at carotid bifurcation (Thomas et al., 2005) or near the bifurcations of coronary arteries (Halon et al., 1983; Frangos et al., 1999).

Since geometry varies among different locations in the vasculature, it is believed that this geometric variation contributes to a corresponding variation in predisposing hemodynamic forces (Lee et al., 2008b). These forces, coming from blood motion, are speculated to play an important role in the initiation and localization of pathologies, which in turn could explain their nonuni-

*Corresponding author, c/Roc Boronat 138, E08018 Barcelona, Spain. Tel: +34 93-542-1448, Fax: +34 93-542-1445
Email addresses: hrvoje.bogunovic@upf.edu (Hrvoje Bogunović), alejandro.frangi@upf.edu (Alejandro F. Frangi)

form distribution (Zhu et al., 2009). Taking this into account, Friedman et al. (Friedman et al., 1983) introduced the concept of "geometric risk factors" as the geometric features that provoke high hemodynamic stresses on the vessel wall.

An important condition for the geometric risk factor concept is the presence of sufficient individual variability in geometry to induce important variations in individual hemodynamics (Friedman, 2002). One vessel of clinical interest that satisfies this requirement is the internal carotid artery (ICA). Located on each side of the neck, ICA is the main vessel that feeds blood to the arteries forming the anterior circulation of the brain. The geometry of ICA varies widely across the population, in particular the part known as the carotid siphon (Krayenbuehl et al., 1982). The carotid siphon (Fig. 1) is the tortuous segment of the ICA that extends from the carotid canal to the terminal bifurcation (ICA-TB) at which the ICA bifurcates into the anterior cerebral artery (ACA) and the middle cerebral artery (MCA).

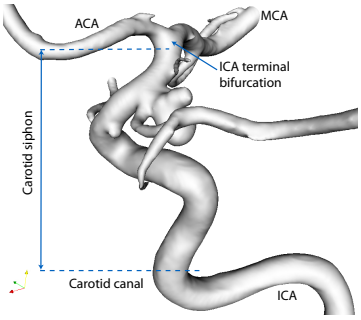

Figure 1: Carotid siphon with an aneurysm on the bifurcation with the posterior communicating artery.

Geometry of ICA is of special interest as incidence rate of aneurysms on it is high, as one third of all intracranial aneurysms occur along the carotid siphon or its terminal bifurcation (Brisman et al., 2006). A couple of studies already identified effects linking geometry and aneurysmal pathology on ICA. Piccinelli et al. (2011) concluded that ICA bends hosting ruptured aneurysms tend to be shorter, having smaller radius, lower maximum curvature, and the aneurysms are located closer to the bend center. Kim and Kang (2007) found that a relatively shorter length of the supraclinoid ICA may be a risk factor for the development of an ICA-posterior communicating artery aneurysm due to higher hemodynamic stress. The geometry of ICA was also of interest to evaluate endovascular accessibility of lesions and for treatment planning, which involves choosing the optimal path and selecting the appropriate type of microcatheters, guidewires and stents (Subramanian et al., 2004; Jiang et al., 2004; Pakbaz and Kerber, 2007; Toyota et al., 2009).

The aim of this work is to provide a methodology for extensive geometric characterization of carotid siphon in an objective, robust and automated way, starting from an angiographic image. The characterization should allow the comparison of carotid siphons within and between subjects and measure their similarity. Such a method would facilitate cataloguing the normal values and the variability of carotid siphon geometry to guide future exploration and identification of specific geometric risk factors.

The summary of the paper is the following. In section 2, we overview the state-of-the-art in the geometric characterization of vasculatures. In section 3, we start presenting the automated characterization pipeline (Fig. 2), with a focus on identifying ICA and detecting anatomical landmarks of carotid siphon. Based on these landmarks of correspondence, we propose two approaches for the geometric characterization (Fig. 2). One is based on computing several geometrically intuitive features (section 4), while the other on measuring the pair-wise similarity between carotid siphons taking their entire shape into account (section 5). In section 7, we validate the automated ICA identification and landmark detection and compare the two characterization approaches in their ability to separate carotid siphons having different shape classes, related to endovascular accessibility. Finally, section 8 discusses the benefits and limitations of the proposed characterization and presents our conclusions.

2. Related work

The geometric characterization of vasculature and in particular of ICA, have already attracted a lot of attention. The state-of-the-art can be divided into two main approaches. The most common one is to represent the vessel shape with a set of geometric indices, which are considered as candidates for being geometric risk factors. The other approach is to consider each point of a centerline as a function of its arc length parameter and then apply functional data analysis (FDA) to explore the variability in a population.

Bullitt et al. (2003, 2005) focused on the measure of tortuosity of the intracerebral vasculature. Three different tortuosity metrics were compared by their effectiveness in detecting several types of abnormalities. In Chen et al. (2002), curvature, torsion and tortuosity and their change along the heart cycle were computed in a selected region of a coronary tree. In Gielecki et al.

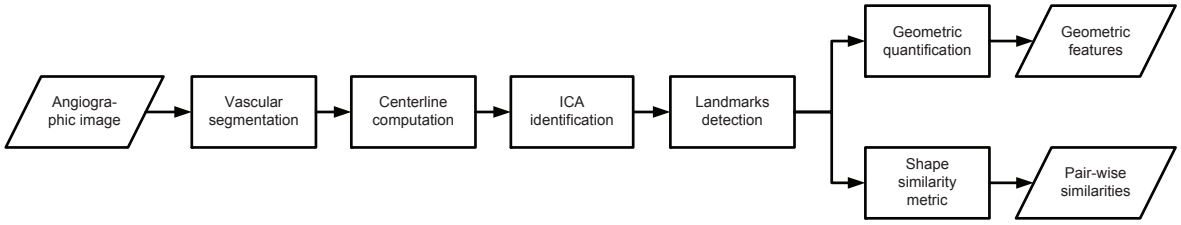

Figure 2: The image-based pipeline for geometric characterization of the carotid siphon.

(2008), tortuosity and deviation index as well as curvature angle were computed for describing the terminal part of the basilar artery. O'Flynn et al. (2007) described the anatomy of normal human abdominal aorta and its side renal arteries with tortuosity, non-planarity of bifurcations, branching angles, curvature and torsion. In the works by Meng et al. (2008a,b), carotid siphon is characterized by its spatial complexity defined as the sum of the curvature and torsion energy. The above methods, apart that they limit the characterization to a small set of isolated geometric indices, require user-interaction.

A framework for geometric analysis of vasculature is presented by Piccinelli et al. (2009). Vascular structures, are objectively characterized using computational geometry. Using such framework, Piccinelli et al. (2011) presented a geometric characterization of ICA and searched for patterns that can be associated to the presence and rupture status of aneurysms. Vessel centerline is partitioned into a sequence of quasi-planar bends. Each bend is then characterized with several geometric indices: torsion peaks at proximal and distal endpoints, mean and maximum curvature, length, radius, angular orientation of aneurysm, etc. However, their method does not guarantee the correspondence of the bends, which is reflected by the discrepancy in the number of bends obtained from different subjects. Furthermore, the number of such obtained bends strongly depends on the applied scale for vessel centerline smoothing.

As opposed to computing geometric indices, Sangalli et al. (2009) applied FDA to characterize a set of centerline curves of ICA. An atlas of curves was created where the reference curve and a set of affine transformations of arc length parameter are simultaneously estimated by Procrustes fitting. From the set of aligned curves, functional principal components analysis (PCA) of their local radius and curvature was performed. In Sangalli et al. (2010), they extended their atlas to allow for multiple reference curves. A method called *k-mean alignment* is proposed for simultaneous alignment and clustering of spatial curves. However, as the transformations are restricted to be affine, the alignment does not assure correspondences between points and bends of curves. These inter-subject anatomical correspondences are essential for computing geometrical descriptors. Besides, we consider them an important requirement for the correct shape comparison between ICAs.

3. ICA segmentation

3.1. Segmentation of the vasculature

Segmentations of the vasculature are performed in an automated way with a geometric deformable model called Geodesic Active Regions (GAR) (Hernandez and Frangi, 2007; Bogunovic et al., 2011). The method was demonstrated to be accurate for 3D rotational angiography (3DRA) and time-of-flight magnetic resonance (TOF-MRA) images. The result of the segmentation is a triangular mesh modeling the vascular lumen with subvoxel precision.

3.2. Vascular tree centerlines computation

The shape of tubular objects, like vessels, can be approximated by the shape of their centerline (medial axis), which is a 3D spatial curve. We obtain the set of vessel centerlines in two steps. First, to obtain the estimate of the topology of the vascular tree, fast topological thinning based on collapsing fronts followed by a fast marching computation to assure centerline connectivity (Cardenes et al., 2010) was applied to obtain the skeleton of the segmentation (Fig. 3). The skeleton, due to imaging resolution and segmentation inaccuracies producing touching vessels, might not have the topology of a tree. However, its end-points do correspond to the root and the terminal leaves of the underlying vascular tree. The root was taken to be the endpoint with the maximal associated radius at the lowest axial plane, which corresponded to the ICA entering the imaged field of view.

Second, the set of accurate centerlines is obtained by backtracking along the minimal cost path from the endpoints toward the root using (Antiga et al., 2003), implemented in the open-source library VMTK (Antiga and

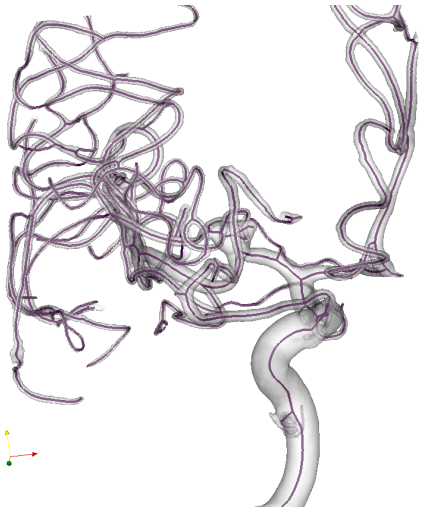

Figure 3: Segmented vascular mesh and its skeleton.

Steinman, 2011). Every point of such centerline, corresponds to the center of a maximally inscribed sphere and the set of centerlines topologically form a rooted tree with the edges directed away from the root in accordance with the blood flow.

3.3. ICA identification

To identify ICA in the extracted vascular tree, we applied the method for detecting ICA-TB, that we preliminarily presented in (Bogunovic et al., 2010). A machine learning based approach is applied, where a classifier is trained on a set of labeled bifurcation feature vectors. Then, a breadth-first traversal of tree bifurcations is performed until the first positive detection. With this strategy we only needed to differentiate ICA-TB from other bifurcations along the ICA as the potential error would appear either as a false positive along the ICA or a false negative at its terminal bifurcation.

Origins of the bifurcations forming the vessel tree and their bifurcation vectors (unit vectors denoting directions of parent vessel and the two daughter branches), are defined using the objective and robust criteria of Antiga and Steinman (2004); Piccinelli et al. (2009). The two daughter branches are differentiated by their radius: the larger daughter branch and the smaller daughter branch. Then, each bifurcation is geometrically characterized with the following 15 dimensional feature vector (Fig. 4(a)): ratios of mean vessel radii between each pair of vessels forming the bifurcation (3); sagittal, axial and coronal-components of the three bifurcation vectors (9); angles between each pair of the bifurcation vectors (3).

As a classifier, we employed $C-$Support vector machine ($C-$SVM) (Chang and Lin, 2011) with a radial basis function kernel. Optimal classifier parameter values were obtained by a simple grid search through multiple combinations. The ones giving the best cross-validation (CV) score were chosen.

Finally, once the ICA-TB is detected, ICA is extracted as a sequence of 4D points (3 spatial centerline coordinates plus the vessel radius) along a curvilinear abscissa starting from the ICA-TB and proceeding toward the heart until it reaches the root of the tree (Fig. 4(b)).

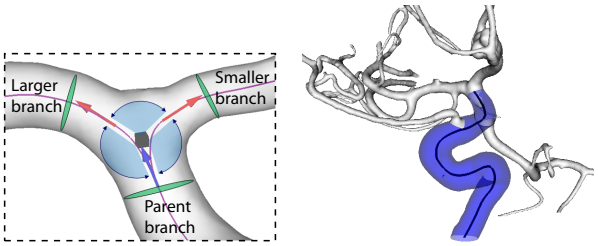

(a) (b)

Figure 4: (a) Bifurcation characterization: Origin (black cube) and associated bifurcation vectors. (b) Example of identified ICA and its centerline.

3.4. Carotid siphon landmarks

To compare carotids within and between subjects, we identify a set of sparse landmark points of anatomical correspondence. They are essential as they will serve as a base for geometric characterization. We model the carotid siphon, the part of ICA from terminal bifurcation to carotid canal, as a sequence of four bends named (from ICA-TB towards the heart): *superior*, *anterior*, *posterior* and *inferior* bend, following their anatomical position with respect to the siphon center (Fig. 5). The inferior, posterior and anterior bends have been observed to be highly planar.For the superior bend, the planar approximation is not found to be valid as its shape resembles more a helix (non-zero torsion).

The landmarks we selected corresponded to: ICA-TB, the centers of the bends and to the interfaces between the bends of the model. However, for the helical superior bend, the location of its center turned out to be highly ambiguous and that landmark has consequently been omitted. The final set of chosen seven landmarks is shown in Fig. 5.

As the landmarks are associated with the four-bend model, we first identify the four bends on a centerline spatial curve. For this, we will make use of two natural frames defined on a spatial curve: The Frenet-Serret

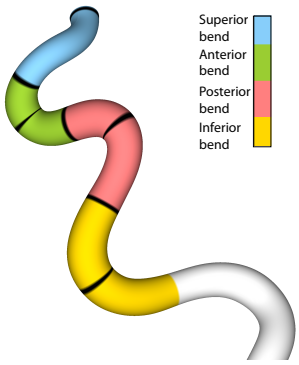

Figure 5: Carotid siphon with the four bends (in color) and the seven landmarks (in black). White area denotes: outside the region of interest.

and the parallel transport one (Bishop, 1975; Hanson and Ma, 1995). We start by giving an overview of the two frames and then present the method for bends and landmarks detection.

3.4.1. Frames on a spatial curve

Given a regular parameterized differentiable space curve Γ with a normalized arc length parameter s,

$$\Gamma = \{\vec{x}(s) | s \in [0,1], \vec{x} \in \mathbb{R}^3\}, \tag{1}$$

the Frenet-Serret frame is defined locally by a triad: tangent $\vec{T}(s)$, normal $\vec{N}(s)$ and binormal $\vec{B}(s)$,

$$\begin{aligned} \vec{T}(s) &= \vec{x}\,'(s) \\ \vec{N}(s) &= \frac{\vec{T}'(s)}{\| \vec{T}'(s) \|} = \frac{\vec{x}\,''(s)}{\| \vec{x}\,''(s) \|} \\ \vec{B}(s) &= \vec{N}(s) \times \vec{T}(s) = \frac{\vec{x}\,'(s) \times \vec{x}\,''(s)}{\| \vec{x}\,'(s) \times \vec{x}\,''(s) \|}. \end{aligned} \tag{2}$$

Thus, $(\vec{T}(s), \vec{N}(s), \vec{B}(s))$ forms an orthonormal basis. $\vec{N}$ is a unit vector pointing towards the center of the locally osculating circle, i.e. in the direction the curve is curved. The vector $\vec{T}'(s) = \kappa(s)\vec{N}(s)$, with the magnitude being the scalar curvature $\kappa(s) = \| \vec{x}\,''(s) \|$, is then called the *curvature vector*. Example of Frenet-Serret frame on a spatial curve is given in Fig. 6(a). Frenet-Serret frame can change orientation abruptly and is not defined when curve is locally straight ($\vec{x}\,''(s) = 0$).

The parallel transport frame (Bishop, 1975), is the frame obtained by parallel transport in the normal bundle of the curve. It can be obtained from any orthonormal basis $\{\vec{E_1}(0), \vec{E_2}(0)\}$ spanning the plane orthogonal to the tangent $\vec{T}(0)$ at the initial point $\vec{x}(0)$, by parallel transporting it along the curve. The following equation defines such a frame:

$$\begin{bmatrix} \vec{T}'(s) \\ \vec{E_1}'(s) \\ \vec{E_2}'(s) \end{bmatrix} = \begin{bmatrix} 0 & k_1(s) & k_2(s) \\ -k_1(s) & 0 & 0 \\ -k_2(s) & 0 & 0 \end{bmatrix} \begin{bmatrix} \vec{T}(s) \\ \vec{E_1}(s) \\ \vec{E_2}(s) \end{bmatrix}. \tag{3}$$

$\vec{E_1}'$ and $\vec{E_2}'$ depend only on $\vec{T}$ and are parallel to it, hence are well defined everywhere on a regular spatial curve, regardless of curvature. Example is given in Fig. 6(b). Such frame is smoothly varying and not affected by the underlying torsion.

We are interested in representing the curvature vector in the parallel transport frame:

$$\vec{T}'(s) = \kappa(s)\vec{N}(s) = k_1(s)\vec{E_1}(s) + k_2(s)\vec{E_2}(s). \tag{4}$$

Thus, k_1 and k_2 are the components of the curvature vector with respect to basis $\{\vec{E_1}, \vec{E_2}\}$ and every spatial curve is uniquely represented in the (k_1, k_2) space up to a rotation. Indeed, this introduces a natural extension to 3D of the notion of the oriented or signed curvature restricted to 2D plane curves. Such a representation avoids the computation of torsion (which requires third-order derivatives), hence we only require curves to be of class C^2, which makes it more stable and robust to the level of noise on the extracted curve.

3.4.2. Bends and landmarks detection

Bends are curved parts of the centerline and are separated by a local curvature minimum at their ends. However, the total number of the curvature extremums varies across population and also depends on the scale and on the extent of ICA visible in the image. To avoid false positive detections due to consecutive curvature minimums forming the same anatomical bend, we will make use of curvature vector expressed in the parallel transport frame. The main idea is to use the property that the curvature vector changes orientation at the bend transitions, while $\vec{E_1}$ and $\vec{E_2}$ of the parallel transport frame remain stable along the curve (Fig. 6(c)). To detect the bend transitions, we then use the curve representation in the above defined (k_1, k_2) space. Thus, the change of bends between two centerline points corresponding to local curvature maximums is expected to produce a wide angle ($\theta > 90°$) between their vectors. On the other hand, if the angle between them is small ($\theta < 45°$), the two curvature maximums are expected to belong to the same bend (Fig. 8(a)).

We argue that this is a more robust approach to bend subdivision than the one based on observing the torsion and curvature peaks along the centerline, presented by Piccinelli et al. (2011). The sensitivity of the torsion

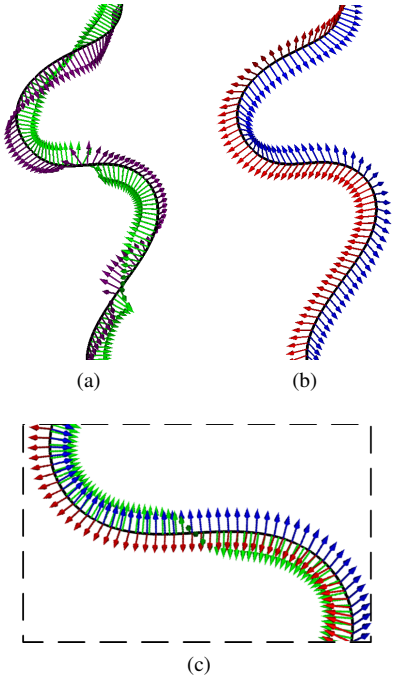

Figure 6: Centerline spatial curve with: (a) Frenet-Serret frame with normal $\vec{N}$ (green) and binormal $\vec{B}$ (purple) vectors. (b) Parallel transport frame with $\vec{E_1}$ and $\vec{E_2}$ (red and blue). (c) Normal vector $\vec{N}$ in the region of bend transition changes the orientation with respect to $\vec{E_1}$ and $\vec{E_2}$.

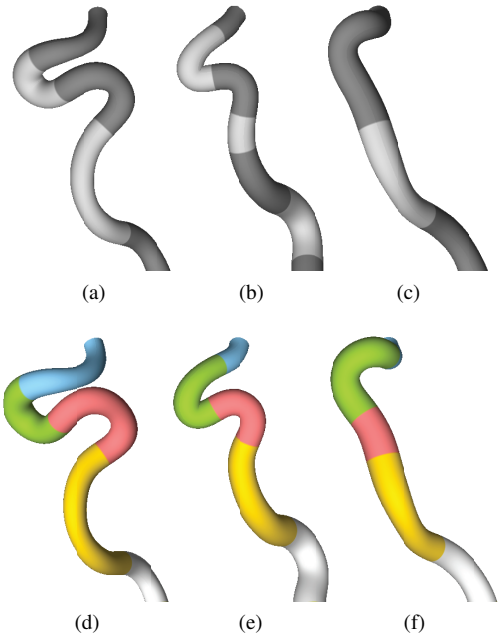

Figure 7: Subdivision of carotid siphon into bends. (a-c) Bend subdivision using the method of Piccinelli et al. (2011) with the same level of Laplacian smoothing of the centerlines. The scale appropriate for case (a), is to small for case (b) and too large for case (c). (e-f) The four bends detected on the same subjects using the proposed method, with fixed, small level of centerline smoothing.

profile to the amount of noise on the centerline makes it difficult to select the level of centerline smoothing, as the level appropriate for one subject is not necessarily appropriate for the others. The proposed representation in (k_1, k_2) space is a more stable approach as the angle between curvature vectors of two centerline points corresponds to the amount (integral) of torsion between them. Detecting bend transitions with a set of angle thresholds was able to consistently identify the corresponding bends across subjects. This is demonstrated in Fig. 7, where the results of the two approaches are compared.

The landmark that will serve as a reference point to identify all four anatomical bends is the one in the middle, marking the interface between the anterior and the posterior bend. It is identified by combining the curvature information with the coronal coordinate of the centerline (Fig. 8(b)). As the anterior bend is anatomically positioned at the front, starting from the position of maximum of the coronal coordinate of the centerline and moving against the blood flow we search for the two neighboring curvature maximum points that have $\theta > \alpha_{\text{ant-post}}$, where $\alpha_{\text{ant-post}}$ is a threshold parameter. The point of curvature minimum between the two such maximums is then the interface landmark.

From the anterior-posterior interface landmark, and moving along the blood flow, we identify the anterior and the superior bends by searching for their interface landmark point as curvature minimum where the two surrounding points of curvature maximums have $\theta > \alpha_{\text{sup-ant}}$. Similarly, moving opposite to the blood flow we identify the posterior-inferior interface landmark with $\alpha_{\text{post-inf}}$. Subsequently, the end of the inferior bend and ROI is found with $\alpha_{\text{inf-end}}$. The threshold parameters were fixed to $\alpha_{\text{ant-post}} = 60°$, $\alpha_{\text{sup-ant}} = \alpha_{\text{post-inf}} = 45°$, and $\alpha_{\text{inf-end}} = 110°$ after observing θ values appearing in a subset of our data.

Once the bends are detected, we estimate their central landmarks. We model the central landmark to correspond to the center of the curved segment of the bend at a scale where its centerline has only one curvature maximum. Thus, if a bend is initially composed of multiple curvature peaks we observe the bend at a larger scale. This is achieved by convolving the centerline curve of the bend with a Gaussian function, as the standard deviation of the Gaussian increases. Such curve evolution is repeated until only one curvature maximum re-

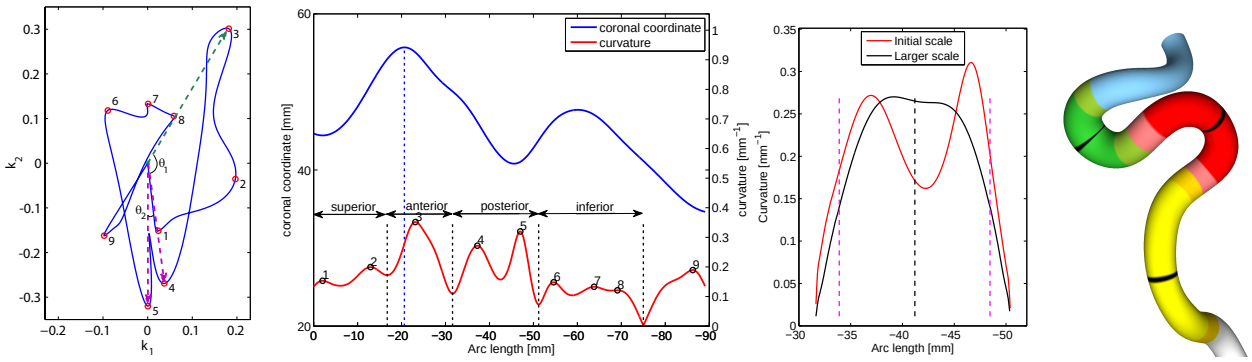

(a) (b) (c) (d)

Figure 8: Bends and landmarks detection: (a) (k_1, k_2) space of the centerline. Numbers denote the curvature peaks sequentially starting from ICA-TB. Between points 3 and 4 ($\theta_1 \approx 120°$) there is a transition of bends. Points 4 and 5 ($\theta_2 \approx 20°$) belong to the same bend (posterior). (b) Coronal coordinate and the curvature of the centerline. The global coronal coordinate maximum is denoted with vertical blue line. The interface landmarks between the four bends are denoted with vertical black lines. (c) Estimation of central segment (bounded with two vertical magenta lines) and central landmark (vertical black line) of the posterior bend, using scale space. (d) The four bends with their central segments (in more saturated color: green, red, yellow) and central landmarks (black).

mains. Then, the central segment is defined as the region around the curvature maximum, delimited on both sides by the mean of the curvature values at the maximum and at the corresponding end. The central landmark is taken as the midpoint of the central segment (Fig. 8(c),(d)).

4. Geometric quantification

Having identified the bends and the landmarks of the carotid siphon, we are now able to compute a set of local and global features that quantify its geometry. As the shape is defined by the object geometry that is invariant under *similarity transformation* (translation, rotation, and uniform scaling) (Kendall et al., 1999), the proposed set of features is accordingly made invariant under this transformation. We compute the following set of geometric features.

4.1. Bend lengths and average vessel radius

Lengths of each of the four bends are presented as percentages of the region of interest occupied by each of the bends, obtained from their normalized arc lengths.

Vessel cross-section area is more related to hemodynamic properties than the radius of the maximally inscribed sphere (Boskamp et al., 2004). Thus, we define as local vessel radius, the radius of a circle having the same cross-section area. Along the centerline of the bend, perpendicular cutting planes are automatically positioned to obtain the vessel cross-sections from the segmented mesh, and the circle equivalent radius is computed. However, if the aspect ratio of minimal over maximal cross-section diameter is below certain threshold (the value of 0.75 is chosen after visual observation), the section is considered to cross an aneurysm or a vessel bifurcation, the cross-section is ignored and its diameter value is linearly interpolated from its neighbors.

4.2. Osculating planes

For the bends that are observed to be quasi-planar (inferior, posterior, anterior), their osculating planes are fitted to the points forming the central segment of each bend using least squares fit. The plane normal vector defined by its sagittal, axial and coronal-components is then used as a feature.

4.3. Change of osculating planes

The bends forming the siphon are concatenated in a non-planar way and the osculating planes change. In general, it has been shown that non-planar connection of double-bend geometries influences the hemodynamics, especially the mixing and swirling of blood flow (Lee et al., 2008a). Thus, we quantify this change of osculating planes of the siphon with the following values:

- Angles between all pairs of osculating plane normal vectors $\vec{n}_i$ computed directly as: $\arccos(\vec{n}_i \cdot \vec{n}_j), i \neq j$.
- Directed angles between osculating plane normal vectors of consecutive bends, computed after parallel transporting one to another on the normal bundle of the curve.

- Two directed angles describing the ouf-of-plane rotation (OPR) of two consecutive bends (*proximal* and *distal*): inferior and posterior; posterior and anterior. One (OPR_1) corresponds to the rotation around the axis lying in the plane of the proximal bend while being orthogonal to the centerline tangent at the transition landmark between the two bends (Fig. 9(a)). The other (OPR_2) corresponds to the rotation around the axis defined by the centerline tangent at the transition landmark between the two bends (Fig. 9(b)).

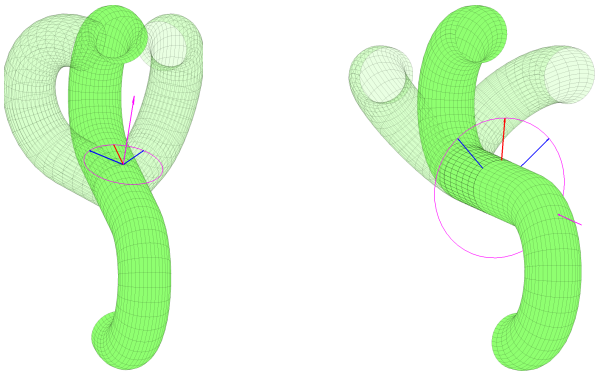

(a) OPR_1 (b) OPR_2

Figure 9: Illustration of the measured change of osculating planes between the posterior and the anterior bend. Each angle (between blue and red vectors) measures the rotation around the corresponding axis (magenta).

4.4. Bending radii

The points of the central segment of each planar bend are fitted with a circle using Gauss-Newton method for non-linear least squares optimization (Fig. 10). Radius of the circle divided by the average vessel diameter of the corresponding bend is then used.

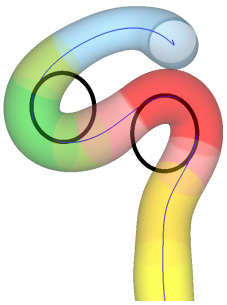

Figure 10: Circles (in black) fitted to the central segments of the anterior and the posterior bends.

4.5. Global features

Global features are computed from the region of interest starting from the terminal bifurcation of ICA until the most proximal landmark (center of the inferior bend). We consider five global features:

Tortuosity Defined as the relative increment in the length of a curve deviating from a rectilinear line, tortuosity χ is computed as (Piccinelli et al., 2009)

$$\chi = \frac{L}{d} - 1, \tag{5}$$

where L is the total arc length of the centerline under analysis and d is the Euclidean distance between its endpoints.

Bending and twisting energy The energy required to bend and twist a straight line into its curved shape. It corresponds to the average value of the square curvature κ and torsion τ, respectively, over the total arc length L of the centerline under analysis. Bending energy (BE) and twisting energy (TE) are defined as (Meng et al., 2008b):

$$\text{BE} = L^2 \int_0^1 \kappa^2(w)dw; \quad \text{TE} = L^2 \int_0^1 \tau^2(w)dw, \tag{6}$$

The L^2 factor guarantees scale invariance.

Curvature ratio and torsion ratio Dimensionless ratios of vessel radius with curvature and torsion radii form part of the Dean and Germano numbers that characterize flows in curved tubes (Formaggia et al., 2009). Thus, we define mean squared curvature ratio (CR) and mean squared torsion ratio (TR) as:

$$\begin{aligned} \text{CR} &= \int_0^1 R^2(w)\kappa^2(w)dw; \\ \text{TR} &= \int_0^1 R^2(w)\tau^2(w)dw, \end{aligned} \tag{7}$$

where, R, κ and τ are local vessel radius, curvature and torsion, respectively.

5. Shape similarity metric

In addition to geometric quantification, we characterize the variability of carotid siphon shapes using the framework of computational anatomy (Grenander and Miller, 1998). There, shape variations are modeled by diffeomorphisms (differentiable transformations with

differentiable inverse). One of the proposed paradigms for diffeomorphic registration is the large deformation diffeomorphic metric mapping (LDDMM) (Beg et al., 2005), which apart from providing correspondences between shapes defines a metric in shape space.

To establish the shape similarity distance measure between carotid siphons, we use the large deformation diffeomorphic metric curve mapping (LDDMCM) (Glaunes et al., 2008), between each pair of their centerline curves. The registration of two spatial curves C and S is performed by searching for a diffeomorphism φ, which matches the given curves: $\varphi(C) = S$, taken as the end point $t = 1$ of a flow of diffeomorphisms ϕ_t modeled by a time-dependent velocity vector field $v_t : \mathbb{R}^d \to \mathbb{R}^d$ as

$$\frac{\partial \phi_t}{\partial t} = v_t(\phi_t); \quad \phi_0(x) = x. \tag{8}$$

The distance between the two curves in the shape space, D(C,S), is then defined by the *length* of the *shortest* diffeomorphism flow matching them:

$$D(C,S) = \inf \rho(\phi_t), \quad \text{when} \quad \phi_0(C) = C, \quad \phi_1(C) = S. \tag{9}$$

The *length* is defined as the deformation cost function

$$\rho(\phi_t) = \left(\int_0^1 \|v_t\|_V dt \right)^{\frac{1}{2}}, \tag{10}$$

where the space V is a reproducing kernel Hilbert space (RKHS) of the smooth velocity fields with reproducing kernel being the Gaussian function with standard deviation σ_V, which determines the smoothness of the deformation.

The optimal transformation $\varphi = \phi_1$ is then computed by minimizing the energy functional

$$J_{C,S}(\phi_t) = \gamma \rho(\phi_t)^2 + E(\phi_1(C), S), \tag{11}$$

where E is a curve matching term and γ is a parameter of regularization weight. The matching term defined in Glaunes et al. (2008) was

$$E_{\text{cr}}(\phi_1(C), S) = \|\mu_{\phi_1(C)} - \mu_S\|^2_{W^*}, \tag{12}$$

where μ_C is a linear functional that embeds the curve C in a RKHS W^* of *currents*, enabling comparison of curves without assuming point correspondences between them. The reproducing kernel is defined by the Gaussian function with standard deviation σ_W, representing a spatial scale of *currents*, and determines the scale of geometric details of curves that are taken into account. σ_W was set to a small value of 2 mm.

We extend the matching term by landmark matching of our previously (subsection 3.4.2) extracted $N = 7$ landmarks $(\vec{x_n}, \vec{y_n}), n = 1, \ldots, N$. This assures anatomically valid matching as the anatomical landmarks are required to correspond. We apply inexact landmark matching (Joshi and Miller, 2000) with normalized Euclidean metric, assuming independency between the landmarks

$$E_{\text{lm}}(\phi_1(\vec{x}), \vec{y}) = \sum_{n=1}^{N} \frac{\|\vec{y_n} - \phi_1(\vec{x_n})\|^2}{\sigma_n^2}, \tag{13}$$

where each landmark n has σ_n associated, which represents the expected inaccuracy in its localization.

Thus, the final energy term that we minimize is

$$J_{C,S,\vec{x},\vec{y}}(\phi_t) = \gamma \rho(\phi_t)^2 + \gamma_{\text{cr}} E_{\text{cr}}(\phi_1(C), S) + \gamma_{\text{lm}} E_{\text{lm}}(\phi_1(\vec{x}), \vec{y}), \tag{14}$$

where γ, γ_{cr}, and γ_{lm} are weights of the regularization, curve matching and landmark matching terms, respectively. As the E_{cr} and E_{lm} matching terms are not symmetric to the choice of source and target curves, neither is the resulting pair-wise distance. To symmetrize it, we take the distance to be the mean value from minimizing $J_{C,S}$ and $J_{S,C}$:

$$D(C,S) = \frac{1}{2}(D(C,S) + D(S,C)). \tag{15}$$

Before the start of the LDDMCM registration, the two curves are registered under the similarity transformation as any variability described by this transformation is not considered as difference in shape. The importance of adding the landmark matching term is demonstrated in Fig. 11. Although the transformed centerlines are similar, the registration without using the landmarks does not provide correct anatomical correspondences of the bends and underestimates the geodesic distance in shape space, compared to the one that does match the landmarks.

6. Evaluation methodology

In this section, the methodology applied for evaluating the elements of the geometric characterization pipeline is presented.

6.1. ICA classification performance

To evaluate the success of ICA-TB identification, 5-fold cross-validation (CV) was repeated 10 times and

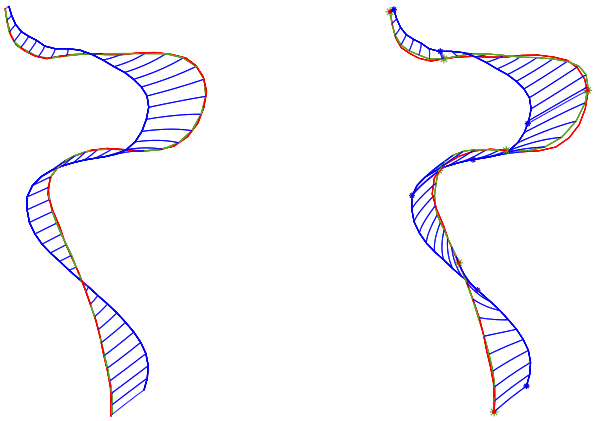

(a) $D = \rho(\phi_t) = 5.7$ (b) $D = \rho(\phi_t) = 6.8$

Figure 11: Diffeomorphic registration of source centerline (blue) to target centerline (red), with the registered centerline (green) and estimated distance D in shape space: (a) without ($E = E_{\text{cr}}$) and (b) with landmark matching term ($E = E_{\text{cr}} + E_{\text{lm}}$).

the estimated accuracy of correct classification was taken as the average CV success rate for all repetitions. To provide a better understanding of which are the most discriminating bifurcation features, we performed feature selection as a sequential forward selection (SFS). Starting with an empty set, at each forward (inclusion) step, the feature added to the feature subset is the one that maximizes the cross-validation (CV) classification rate.

6.2. Landmark detection

As the later geometric characterization is based on the landmarks, their detection has been extensively evaluated both qualitatively and quantitatively.

Qualitative evaluation. First, the carotid siphons were visually inspected to check whether they have been been partitioned into the four bends and that none of them were merged or split. Second, to evaluate the stability of the thresholds chosen for the four bends of the model, we displayed the probability densities of angles θ in (k_1, k_2) space (Fig. 8(a)) between curvature maximums that belonged to the true and false transitions.

Quantitative evaluation. The landmarks from the four-bend model attempt to reproduce the human intuition of where are the corresponding points representing bend transitions and their centers. As the model is just an approximation of objects having much larger anatomical variability, these points do not necessarily coincide with the curvature properties like the maximum and minimum. Thus, we considered expert observer as the best reference for identifying these corresponding points along the siphon. The reference landmark positions were obtained as the average across multiple observers of the manually placed ones. To evaluate the accuracy of the automatically determined landmarks we then computed:

- The *limits of agreement* of the automatically determined landmarks with the reference, which represent the 95% confidence interval of the differences (Bland and Altman, 1986) and are expressed as bias and standard deviation σ_{loa}.
- The standard deviation of the inter-observer variability σ_{o}, computed using one-way analysis of variance (ANOVA) (Carstensen et al., 2008).
- The variability index I, defined as the ratio of the above two standard deviations:

$$I = \frac{\sigma_{\text{loa}}}{\sigma_{\text{o}}}. \tag{16}$$

  If the value of this index $I < 1$, the landmarks from the automated method deviate from the reference less than the manually placed landmarks vary between observers.

6.3. Geometric quantification

The values of the computed geometric features (section 4) depend on the estimated landmark positions. Thus, we compared the values of features computed from automatically determined landmarks to the ones obtained with manually placed landmarks. Reference is taken to be the average of the values obtained from individual landmarkings by each observer. We then computed for each feature the variability index I (Eq. 16) and the normalized mean error computed as absolute error divided by the population range of values.

6.4. Shape similarity metric

The pairwise shape similarities also depend on the estimated landmark positions. We take the reference to be the shape distances obtained using the reference landmark positions and enforcing the exact landmark matching during the registration process. Exact landmark matching is enforced by setting a high value to the weight γ_{lm} in Eq. 14. The distances based on automated landmarking were then computed with three different options for the landmark matching terms: no landmark matching, exact landmark matching, and the proposed inexact landmark matching. The limits of agreement

with the reference for these three variants are computed and compared. In addition, we evaluated how different choices of the parameter σ_V, which defines the smoothness of the deformation field, affect the obtained distances and the matching residuals (Eq. 11).

6.5. Carotid siphon shape classes

To evaluate and compare the characterizations based on the proposed geometric features and LDDMCM, two clinicians labeled the class of siphon shape following the classification proposed by Krayenbuehl et al. (1982). Such classification has been used in evaluating the vascular accessibility between the guide-catheter and the lesion (Kim et al., 2008). Essentially, there are four shape classes: U, C, V and S (Fig. 12), with variation being mainly in the part of the anterior and the posterior bend. We then expect that the siphons characterized by the two proposed schemes will cluster by classes i.e. the siphons belonging to the same class will have similar geometric features and small LDDMCM distance to each other.

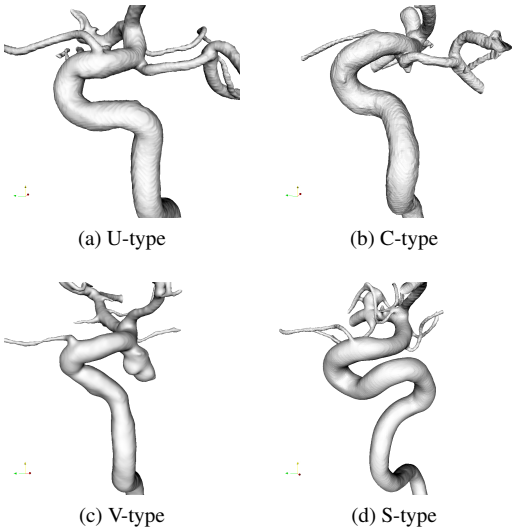

(a) U-type (b) C-type

(c) V-type (d) S-type

Figure 12: Examples of carotid siphon shape classes.

The following steps were then performed. First, we applied dimensionality reduction to map all the carotid siphons to an Euclidean submanifold. Principal Geodesic Analysis (PGA) (Fletcher et al., 2004) is applied on the geometric features as they are composed of a mixture of features in $\mathbb{R}^+$ (radii and lengths), SO(2) (angles), and S^2 (normal vectors). Each normal vector is treated as a single feature, having two degrees of freedom. Similarly, for LDDMCM, classical multidimensional scaling (CMDS) (Pekalska and Duin, 2005) is applied. We performed two dimensionality reductions. One to 2D, for the purpose of visualizing and qualitatively evaluating the achieved clustering. The other, to a smallest dimension still preserving the 99% of the total data variance, for the purpose of quantitative evaluation as a classification success rate of a linear classifier. In the obtained submanifold, we trained a classifier using linear discriminant analysis (LDA) and leave-one-out cross-validation classification rate is reported as a measure of how well separated the four classes are. Finally, we looked at the LDDMCM classification performance for different choices of σ_V while for the characterization based on geometric features we performed SFS of features to identify the most relevant ones.

7. Results

The geometric characterization pipeline was retrospectively applied to 96 images acquired with 3DRA, from 86 patients (age range: 33 – 76, mean age: 53 years, 74% women). Contrast was injected to enhance the vessels comprising anterior cerebral circulation of either left (43) or right (53) hemisphere (10 patients had both sides imaged). Acquisitions were performed with an angiographic unit: Allura Xper FD20 (Philips Healthcare, Best, The Netherlands). On a dedicated workstation, 3D images were reconstructed with a 256^3 matrix having a voxel size of $0.29 \times 0.29 \times 0.29$ (mm). All images were successfully segmented and had their vascular tree centerlines and topology extracted.

7.1. ICA classification performance

From all 96 vascular trees, the feature vectors of 297 bifurcations along ICA were manually labeled as "terminal" (96) or "non-terminal" (201), and supplied to SVM classifier for training and cross-validation (CV) (Fig. 13). Feature selection revealed that the two features that contributed the most to the ICA-TB discrimination were: *ratio of mean radii between the smaller and the larger daughter branches* and *axial component of the smaller daughter branch vector*. At peak CV rate (6 selected features) ICA-TB was misclassified in only one case (99% success) rate, producing one false positive and zero false negatives (99.5% specificity and 100% sensitivity). The false positive sample was the only example available of a bifurcation of ICA with a tentorial marginal branch, hence during its testing none were present in the training data. The results show that the chosen features describe adequately the bifurcation.

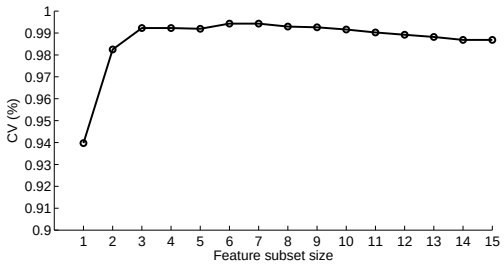

Figure 13: Identification of ICA-TB: Cross-validation (CV) classification rates for sequential forward selection of features.

7.2. Landmark detection

Qualitative evaluation. Detection of landmarks for partitioning the carotid siphon into bends failed in three cases (97% success rate) (Fig. 14). Failure occurred mostly when the transition between the posterior and the inferior bend was missed due to small angle between vectors in (k_1, k_2) space ($\theta < \alpha_{\text{post-inf}} = 45°$, Fig. 14(d)).

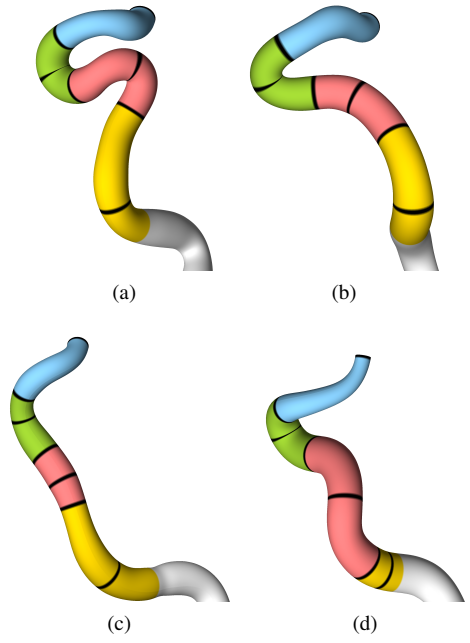

Figure 14: Automated landmarking:(a-c) Examples of successful cases. (d) Example of a case where the posterior and the inferior bend were incorrectly detected as one ($\theta_{\text{post-inf}} = 40°$).

Evaluation of threshold stability is shown in Fig. 15. Of the four thresholds, the $\alpha_{\text{ant-post}}$, $\alpha_{\text{inf-end}}$ are the more stable ones, as they separate two distributions tightly grouped around their means. We can observe that any choice of $\alpha_{\text{ant-post}}$ in the range of $[40^o - 80^o]$ would produce the same results. Choice of $\alpha_{\text{post-inf}}$ and $\alpha_{\text{ant-sup}}$ is more critical but given that they were evaluated on a large number of cases, a good generalization is expected.

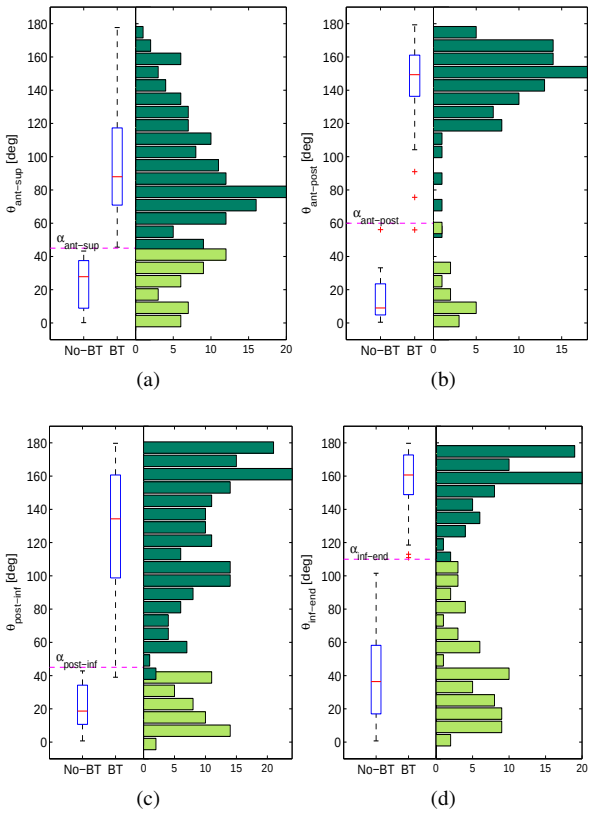

Figure 15: Distribution of angles in (k_1, k_2) space that present bend transition (BT) and non-bend transition (No-BT), in a form of a boxplot and histogram. (a) anterior-superior, (b) anterior-posterior, (c) posterior-inferior, (d) inferior-end.

Quantitative evaluation. Three observers manually placed the landmarks on sequentially chosen subset of 50 cases. The results are shown in Fig. 16. The transition between the superior and the anterior bend (L1) has the largest localization error in both bias and standard deviation. However, this is the location with the largest inter-observer variability as well. For other landmarks, either the bias is not statistically significant or the variability is within 50% of the inter-observer one. The central landmarks (L2, L4, L6) are particularly well detected with no significant bias and the deviation from the reference being below the inter-observer one for the posterior and the inferior bends.

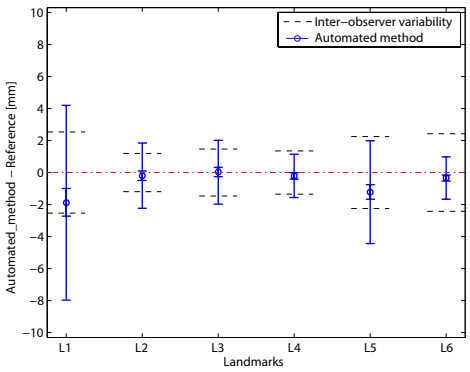

(a)

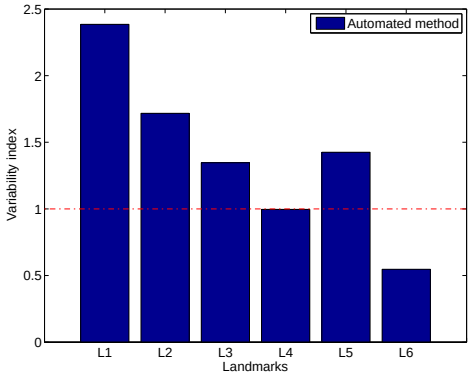

(b)

Figure 16: (a) Limits of agreement between automated landmarking and the reference. Bias is denoted with a marker and 95% confidence interval, while the bars correspond to 95% limits of agreement ($\pm 2\sigma_{\text{loa}}$). Agreements are compared with inter-observer limits of agreement for the manual measurements (b) Variability index for each landmark. Landmarks are ordered from distal to proximal: superior-anterior (L1), central anterior (L2), anterior-posterior (L3), central posterior (L4), posterior-inferior (L5) and central inferior (L6).

7.3. Geometric quantification

The evaluation results for the total set of geometric features is shown in Fig. 17. We can observe that all the features have $I < 1.8$ and normalized mean absolute error below 8% with more than half of them having $I < 1.3$ and error less than 3%. Thus, we can assume that landmark localization is sufficiently accurate not to affect the computed geometric features.

7.4. Shape similarity metric

For the registrations using inexact landmark matching, previously evaluated σ_{loa} (Fig. 16(a)) of each landmark's limits of agreement are used to normalize corresponding Euclidean distances ($\sigma_n = \sigma_n^{\text{loa}}$) in Eq. 13. Thus, the larger the landmark's discrepancy from the

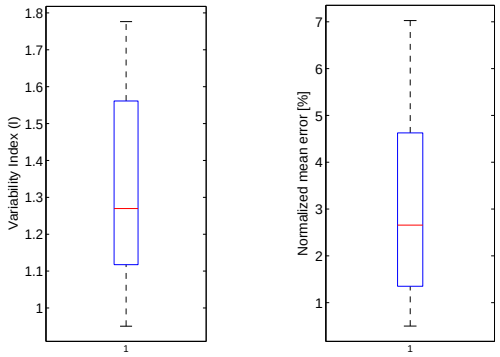

(a) (b)

Figure 17: Boxplot for geometric features, showing the distribution of: (a) variability index and (b) normalized mean error. Boxes span the lower (higher) quartiles and whiskers extend up to 1.5 the interquartile range.

reference, the smaller is its influence during the registration.

The parameters γ_{cr} and γ were experimentally set to $\gamma_{\text{cr}} = 1$ and $\gamma = 0.1$, for all registrations. Observing the effect of the parameter σ_V on the registration results, for large σ_V (> 6 mm), due to strong smoothness constraint on the deformation, the final matching precision deteriorates. At such scales, the deformation is not accounting for the details that we consider to be part of the difference in geometry as opposed to noise. Small σ_V (< 1 mm), allows highly irregular speed fields and nearby regions start to move independently. The obtained distance is not representative of the one in the shape space and the registration optimization is likely to end in a local minimum. The analysis (Fig. 18) confirms this observation. The values of σ_V from the range $[1, 6]$ produce small matching error and the optimal choice depends on a priori assumptions and the final application. We chose $\sigma_V = 4.5$ mm, which is the scale of the average vessel diameter. This choice is later reevaluated for the application to siphon shape classification.

For the inexact landmark matching, to find γ_{lm} we took a small sample of the first 10 cases and used it as a training set. Then, the sweep search with $\gamma_{\text{lm}} = \{2^{-3}, \ldots, 2^3\}$ was performed and the value that produced the best agreement with the reference was used ($\gamma_{\text{lm}} = 1$).

To compare the results with the three different landmark matching terms, the distances based on automated landmarking were then computed with: no landmark matching ($\gamma_{\text{lm}} = 0$), exact landmark matching ($\gamma_{\text{lm}} = 100$), and the proposed inexact landmark matching ($\gamma_{\text{lm}} = 1$). The limits of agreement with the ref-

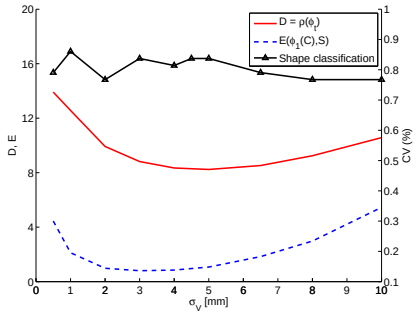

Figure 18: Sensitivity to the parameter σ_V of: The distance D, the matching residual E after the registration with inexact landmark matching (average curves across pair-wise registrations), and the cross-validation (CV) siphon shape classification rate.

erence for these three variants are shown in Fig. 19. We can observe: First, that using landmarks is important as otherwise the obtained similarity distances are underestimated. Second, using the proposed inexact landmark matching showed improvements in terms of smaller bias and standard deviation compared to enforcing exact landmark matching, since any inaccuracies in landmark localization influence less the registration process. The distances obtained with inexact landmark matching had the variability index $I = 1.1$, which is close to the variability obtained with the manual landmarking.

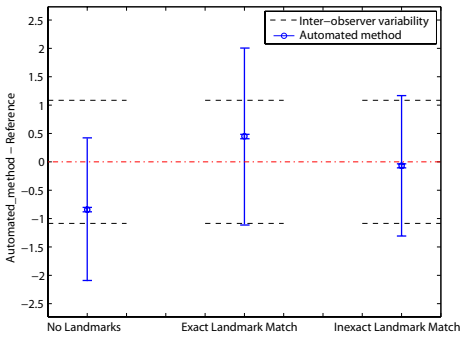

Figure 19: Limits of agreements of distances based on automated landmarking with the reference distances. Results for LDDMCM with the three types of landmark matching terms are shown: None, exact and inexact.

7.5. Carotid siphon shape classes

As many siphons had ambiguous shape, only the ones where both clinicians agreed on the shape class were used (43 cases). The first step in the evaluation is the dimensionality reduction and we look at the residual variances as a measure of the obtained statistical fit (Fig. 20(a)). Residual variance is defined as $1-R^2$, where R is the correlation coefficient between the pairwise point distances in a subspace and the original space. We can observe that the items with characterization based on the LDDMCM can be better represented in a low dimension ($< 5D$) than the ones characterized by the geometric features. For other dimensionality reductions, both characterizations produce similar residual variances and the more dimensions used, the better the statistical fit.

Observing, the items mapped to a 2D Euclidean submanifold (Fig. 20(b)&(c)), LDDMCM appears to produce more discriminating clusters than the geometric features. This is confirmed by the classification of labeled items mapped to a 12-dimensional submanifold (where residual variance for both approaches is negligible), as there $CV_{\text{LDDMCM}} = 84\%$ while $CV_{\text{Features}} = 63\%$. To further evaluate the importance of using landmark matching in the registration process, we computed the CV rate for the results obtained without the landmark matching term: $CV_{\text{LDDMCM\_no\_landmarks}} = 77\%$, which produced worse class separability than the proposed method.

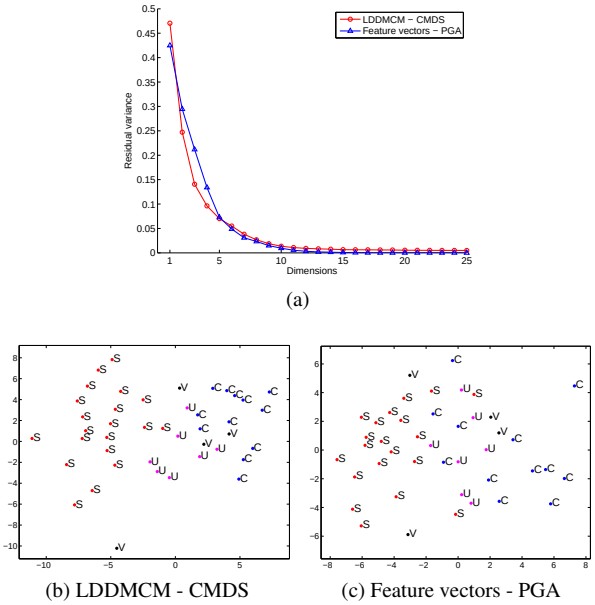

Figure 20: Dimensionality reduction to a submanifold. (a) Comparison of residual variances after dimensionality reduction. (b,c) Items mapped to a 2D Euclidean submanifold, with labels denoting siphon shape classes.

LDDMCM classification for different choice of σ_V parameter (Fig. 18), shows that the performance is very stable in the range $[3, 5]$ mm, and still quite stable (77%-86%) in the entire evaluated range $[0.5, 10]$ mm. The results of geometric feature selection are shown in Fig. 21.

Using the feature selection improves the CV rate and the peak $CV_{\text{Features}} = 77\%$ is reached already with four features. The four features in the order of importance were: *tortuosity*, *normal vector of the anterior bend's osculating plane*, *length of the anterior bend* and the *bending radius of the anterior bend*. This is in good agreement with the visually observed variability of shape types, which is mostly due to the change in the geometry of the anterior and the posterior bends.

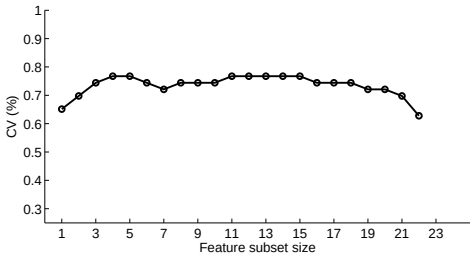

Figure 21: Siphon shape classification: Cross-validation (CV) classification rates for sequential forward selection of geometric features.

8. Discussion and conclusions

We presented a pipeline for extensive geometric characterization of carotid siphon. Starting from angiographic image the pipeline identifies and extracts the centerline and radius of the ICA. On the extracted centerline we automatically detect anatomical landmarks of the region of interest corresponding to carotid siphon, which are prerequisites for the proposed geometric characterization. Landmarks as points of anatomical correspondence are used for computing both: geometric features and LDDMCM shape similarity.

The method to identify ICA from a vascular tree by detecting ICA-TB had a high classification success rate (99%). Looking at the two most discriminative features: *ratio of mean radii between the smaller and the larger daughter branches* and *axial component of the smaller branch vector*, the classifier learned that ICA-TB branches into two similarly big vessels as opposed to a narrow side vessel and also that the smaller branch vector (corresponding to ACA) is pointing towards the top of the head.

One of the main elements of the paper was automated landmark detection as it is essential for later characterization. Landmarks were associated to the four bend model of the carotid siphon. Apart from the superior bend, the other three bends were modeled as planar. An alternative would be to split the superior bend into two smaller quasi-planar bends, but we observed that those two bends are not consistently present between subjects. Direct application of the bend detection method by Piccinelli et al. (2011), which uses curvature and torsion centerline profiles, was not suitable as it does not assure bend correspondences and the results are sensitive to the applied centerline smoothing scale. Thus, a more robust method, based on the curvature vector expressed in the parallel transport frame is proposed.

Landmarks are essential for geometric features as they define, in an automated and consistent manner, the corresponding regions of interest for local and global features. They are crucial for computing LDDMCM as they assure anatomically correct registrations. The validation study showed that the automatically obtained landmarks are in agreement with the ones selected manually and that they do not affect the obtained geometric quantities or LDDMCM distances with respect to manual landmarking. Using automated approach avoids observer variability and enables high reproducibility among a set of individuals, which is imperative in performing robust population studies.

The presented set of geometric features were selected from typical geometric quantities used in the literature, known to affect hemodynamics. In general, they should be defined and selected in accordance to the hypothesis one is testing. Characterization based on geometric features and LDDMCM are two complementary approaches. The former has the advantage that any observed associations or variabilities of features are straightforward to interpret. The later quantifies shape differences directly hence is more effective in capturing subtle changes in geometry but its interpretation is more abstract. Both approaches avoid the need for any point correspondences, apart from the sparse set of anatomical landmarks.

The explanatory power of the characterization was evaluated by observing the discrimination of siphon shape classes in the submanifold coordinates, seen as modes of anatomical variation of population. The characterization based on LDDMCM proved better in classifying the carotid siphon shape classes than the one based on geometric features. These shape classes already have direct clinical relevance in selecting the endovascular treatment strategy, but they could be replaced by any other clinical condition of interest, e.g. presence of aneurysm or its rupture status. Then, insights about the relation of the geometry of carotid siphon with its clinical condition could be obtained and automatically quantified in a large population.

The proposed methodology has limitations. As we assume all carotid siphons can be modeled with the four bends, the landmarking fails when two neighbor-

ing bends are perceived as one large bend. In our database, this assumption was rarely violated (3%). In general, the method could be extended to learn the geometric properties of the bends, to detect unrealistic (unprobable) solutions. Regarding the computation of LDDMCM similarities, the drawback of the registration metric is that it is not symmetric with respect to the source and target curves. Thus, the resulting shape distance was taken as the mean value from the two registrations. In addition, adding a new case requires registering it with all the cases from the database. For a limited size database, like ours, this is not a problem, as the registration of spatial curves is generally much faster than the registration of volumetric images. In the case of larger datasets, a low-dimensional manifold could be first learned from a set of curves used as a training set. Then, each new centerline curve would be projected directly on the manifold, as similarly presented for brain images in Gerber et al. (2010).

8.1. Conclusions and Outlook

Geometry of carotid siphon has a large variability across subjects, which makes it a good candidate to be a potential risk factor for the onset of vascular pathologies on and off the ICA. We have presented a complete and automated pipeline for geometric characterization of the carotid siphon. The proposed approach, based on anatomical landmarks, enables the analysis through a set of geometric features and LDDMCM shape similarities.

Some elements of the proposed pipeline are new and represent contributions in themselves. In this sense, the main contributions of the paper are the following:

- Algorithm for the automated identification of ICA-TB and its discriminating features.
- Algorithm for the automated detection of vessel bends based on the curvature vector expressed in the parallel transport frame and its application to anatomical landmarking of carotid siphon.
- Definition and computation of geometric quantities like angles of rotation between osculating planes of consecutive bends, having a known influence on hemodynamics.
- The use of LDDMCM similarity metric for vessels and the importance of using the inexact landmark matching to obtain anatomically valid deformations.

Although the methodology is tuned to carotid siphons, it is applicable to other vessels. The classifier used for the identification of ICA can be extended to detect more bifurcations for the purpose of anatomical labeling of the vascular tree and this is currently under study. The bend identification algorithm and the geometric quantities defined on them are generic and can be applied to any vessel (e.g. aorta, coronaries or peripheral arteries) or tubular structure. However, the number and the type of bends might not be as consistent along the population as they are for the carotid siphon. In that case, classical LDDMCM, without the landmarks, can be used as a shape similarity metric and the number of bends can then become a geometric feature in itself.

The presented characterization is the first step in the pursuit of geometric risk factors of carotid siphon. Identifying these factors was not the aim of this paper, but will form part of the future work. In addition, the techniques used here will be extended to a more distal level, in an effort to characterize the complete Circle of Willis.

Acknowledgments

This work was partially supported by the CENIT programme of CDTI, the Industrial and Technological Development Centre of Spain, under the research project cvREMOD (CEN-20091044), and by Philips Healthcare B.V. (Best, The Netherlands). H. Bogunović is supported by the FI-DGR 2009 fellowship of AGAUR and R. Cárdenes by the Beatriu de Pinós programme of AGAUR. A.F. Frangi holds an ICREA-Academia Award by the Institutció Catalana de Recerca i Estudis Avançats (ICREA).

Antiga, L., Ene-Iordache, B., Remuzzi, A., 2003. Computational geometry for patient-specific reconstruction and meshing of blood vessels from MR and CT angiography. IEEE Trans. Med. Imag. 22, 674–684.

Antiga, L., Steinman, D.A., 2004. Robust and objective decomposition and mapping of bifurcating vessels. IEEE Trans. Med. Imag. 23, 704–713.

Antiga, L., Steinman, D.A., 2011. VMTK: the Vascular Modeling Toolkit. http://www.vmtk.org.

Beg, M.F., Miller, M.I., Trouve, A., Younes, L., 2005. Computing large deformation metric mappings via geodesic flows of diffeomorphisms. Int. J. Comput. Vis. 61, 139–157.

Bishop, R.L., 1975. There is more than one way to frame a curve. Am. Math. Monthly 82, 246–251.

Bland, J.M., Altman, D.G., 1986. Statistical methods for assessing agreement between two methods of clinical measurement. Lancet 327, 307–310.

Bogunovic, H., Pozo, J.M., Cardenes, R., Frangi, A.F., 2010. Automatic identification of internal carotid artery from 3DRA images, in: Proc. Int. Conf. IEEE Eng. Med. Biol. Soc. (EMBC), pp. 5343–5346.

Bogunovic, H., Pozo, J.M., Villa-Uriol, M.C., Majoie, C.B.L.M., van den Berg, R., Gratama van Andel, H.A.F., Macho, J.M., Blasco, J., San Roman, L., Frangi, A.F., 2011. Automated segmentation of cerebral vasculature with aneurysms in 3DRA and TOF-

MRA using geodesic active regions: An evaluation study. Med. Phys. 38, 210–222.

Boskamp, T., Rinck, D., Link, F., Kmmerlen, B., Stamm, G., Mildenberger, P., 2004. New vessel analysis tool for morphometric quantification and visualization of vessels in CT and MR imaging data sets. RadioGraphics 24, 287–297.

Brisman, J.L., Song, J.K., Newell, D.W., 2006. Cerebral aneurysms. N. Engl. J. Med. 355, 928–939.

Bullitt, E., Gerig, G., Pizer, S.M., Lin, W., Aylward, S.R., 2003. Measuring tortuosity of the intracerebral vasculature from MRA images. IEEE Trans. Med. Imag. 22, 1163–1171.

Bullitt, E., Muller, K.E., Jung, I., Lin, W., Aylward, S., 2005. Analyzing attributes of vessel populations. Med. Image Anal. 9, 39–49.

Cardenes, R., Bogunovic, H., Frangi, A.F., 2010. Fast 3D centerline computation for tubular structures by front collapsing and fast marching, in: Proc. IEEE Int. Conf. Image Process. (ICIP), pp. 4109–4112.

Carstensen, B., Simpson, J., Gurrin, L.C., 2008. Statistical models for assessing agreement in method comparison studies with replicate measurements. Int. J. Biostat. 4. Article 16.

Chang, C.C., Lin, C.J., 2011. LIBSVM: a library for support vector machines. http://www.csie.ntu.edu.tw/~cjlin/libsvm.

Chen, S.Y.J., Carroll, J.D., Messenger, J.C., 2002. Quantitative analysis of reconstructed 3-D coronary arterial tree and intracoronary devices. IEEE Trans. Med. Imag. 21, 724–740.

Fletcher, P., Lu, C., Pizer, S., Joshi, S., 2004. Principal geodesic analysis for the study of nonlinear statistics of shape. IEEE Trans. Med. Imag. 23, 995–1005.

Formaggia, L., Quarteroni, A., Veneziani, A., 2009. Cardiovascular Mathematics: Modeling and simulation of the circulatory system. Springer.

Frangos, S.G., Gahtan, V., Sumpio, B., 1999. Localization of atherosclerosis: role of hemodynamics. Arch. Surg. 134, 1142–1149.

Friedman, M.H., 2002. Variability of 3D arterial geometry and dynamics, and its pathologic implications. Biorheology 39, 513–517.

Friedman, M.H., Deters, O.J., Mark, F.F., Bargeron, C.B., Hutchins, G.M., 1983. Arterial geometry affects hemodynamics. a potential risk factor for atherosclerosis. Atherosclerosis 46, 225–231.

Gerber, S., Tasdizen, T., Thomas Fletcher, P., Joshi, S., Whitaker, R., 2010. Manifold modeling for brain population analysis. Med. Image Anal. 14, 643–653.

Gielecki, J., Zurada, A., Gajda, G., Nowak, D., Sienkiewicz-Zawilinska, J., 2008. The description of vascular variations in three-dimensional space: a novel method of spatial cerebral arteries evaluation. Med. Sci. Mon. 14, MT36.

Glaunes, J., Qiu, A., Miller, M.I., Younes, L., 2008. Large deformation diffeomorphic metric curve mapping. Int. J. Comput. Vis. 80, 317–336.

Grenander, U., Miller, M.I., 1998. Computational anatomy: An emerging discipline. Q. Appl. Math. 56, 617–694.

Halon, D.A., Sapoznikov, D., Lewis, B.S., Gotsman, M.S., 1983. Localization of lesions in the coronary circulation. Am. J. Cardiol. 52, 921–926.

Hanson, A.J., Ma, H., 1995. Quaternion frame approach to streamline visualization. IEEE Trans. Vis. Comput. Graphics 1, 164–174.

Hernandez, M., Frangi, A., 2007. Non-parametric geodesic active regions: method and evaluation for cerebral aneurysms segmentation in 3DRA and CTA. Med. Image Anal. 11, 224–241.

Jiang, W.J., Wang, Y.J., Du, B., Wang, S.X., Wang, G.H., Jin, M., Dai, J.P., 2004. Stenting of symptomatic M1 stenosis of middle cerebral artery: an initial experience of 40 patients. Stroke 35, 1375–1380.

Joshi, S.C., Miller, M.I., 2000. Landmark matching via large deformation diffeomorphisms. IEEE Trans. Image Process. 9, 1357–70.

Kendall, D.G., Barden, D., Carne, T.K., Le, H., 1999. Shape and Shape Theory. Wiley.

Kim, D.W., Kang, S.D., 2007. Association between internal carotid artery morphometry and posterior communicating artery aneurysm. Yonsei Med. J. 48, 634–8.

Kim, J.S., Caplan, L.R., Wong, K.S.L., 2008. Intracranial Atherosclerosis. Wiley-Blackwell.

Krayenbuehl, H., Yasargil, M., Huber, P., 1982. Cerebral Angiography. Thieme. 2nd edition edition.

Lee, K.E., Parker, K.H., Caro, C.G., Sherwin, S.J., 2008a. The spectral/ hp element modelling of steady flow in non-planar double bends. Int. J. Numer. Meth. Fluid 57, 519–529.

Lee, S.W., Antiga, L., Spence, J.D., Steinman, D.A., 2008b. Geometry of the carotid bifurcation predicts its exposure to disturbed flow. Stroke 39, 2341–2347.

Meng, S., Costa, L.d.F., Geyer, S.H., Viana, M.P., Reiter, C., Muller, G.B., Weninger, W.J., 2008a. Three-dimensional description and mathematical characterization of the parasellar internal carotid artery in human infants. J. Anat. 212, 636–644.

Meng, S., Geyer, S.H., Costa, L.d.F., Viana, M.P., Weninger, W.J., 2008b. Objective characterization of the course of the parasellar internal carotid artery using mathematical tools. Surg. Radiol. Anat. 30, 519–526.

O'Flynn, P.M., O'Sullivan, G., Pandit, A.S., 2007. Methods for three-dimensional geometric characterization of the arterial vasculature. Ann. Biomed. Eng. 35, 1368–1381.

Pakbaz, R.S., Kerber, C.W., 2007. Complex curve microcatheters for berry aneurysm endovascular therapy. AJNR Am. J. Neuroradiol. 28, 179–180.

Pekalska, E., Duin, R.P.W., 2005. The Dissimilarity Representation for Pattern Recognition: Foundations and Applications. World Scientific Publishing Company.

Piccinelli, M., Bacigaluppi, S., Boccardi, E., Ene-Iordache, B., Remuzzi, A., Veneziani, A., Antiga, L., 2011. Geometry of the ICA and recurrent patterns in location, orientation and rupture status of lateral aneurysms: an image-based computational study. Neurosurgery 68, 1270–1285.

Piccinelli, M., Veneziani, A., Steinman, D.A., Remuzzi, A., Antiga, L., 2009. A framework for geometric analysis of vascular structures: application to cerebral aneurysms. IEEE Trans. Med. Imag. 28, 1141–1155.

Sangalli, L.M., Secchi, P., Vantini, S., Veneziani, A., 2009. A case study in exploratory functional data analysis: Geometrical features of the internal carotid artery. J. Am. Stat. Assoc. 104, 37–48.

Sangalli, L.M., Secchi, P., Vantini, S., Vitelli, V., 2010. K-mean alignment for curve clustering. Comput. Stat. Data Anal. 54, 1219–1233.

Subramanian, N., Kesavadas, T., Hoffmann, K., 2004. Geometry-based metrics for planning of neuroendovascular therapy, in: Lemke, H.U., Inamura, K., Doi, K., Vannier, M.W., Farman, A.G., Reiber, J.H.C. (Eds.), Proc. Int. Congr. Comput. Assist. Radiol. Surg. (CARS), pp. 718–723.

Thomas, J.B., Antiga, L., Che, S.L., Milner, J.S., Steinman, D.A.H., Spence, J.D., Rutt, B.K., Steinman, D.A., 2005. Variation in the carotid bifurcation geometry of young versus older adults: implications for geometric risk of atherosclerosis. Stroke 36, 2450–2456.

Toyota, S., Fujimoto, Y., Iwamoto, F., Wakayama, A., Yoshimine, T., 2009. Technique for shaping microcatheter tips in coil embolization of paraclinoid aneurysms using full-scale volume rendering images of 3D rotational angiography. Minim. Invasive Neurosurg. 52, 201–203.

Zhu, H., Ding, Z., Piana, R.N., Gehrig, T.R., Friedman, M.H., 2009. Cataloguing the geometry of the human coronary arteries: a potential tool for predicting risk of coronary artery disease. Int. J. Cardiol. 135, 43–52.